

LARGE SCALE STRUCTURES AND NOISE GENERATION IN LEADING EDGE SLAT OF HIGH LIFT AIRFOILS

Daniel S. Souza, dss-em@usp.br

Universidade de São Paulo, Rua João Dagnone, 1100, São Carlos - Brasil

Daniel Rodríguez, dani@mec.uff.br

Departamento de Engenharia Mecaânica, Pós-Graduação em Eng. Mecânica (PGMEC), Universidade Federal Fluminense, Rua Passo da Pátria, 156, Rio de Janeiro - Brasil

Marcello A. F. Medeiros, marcello@sc.usp.br

Universidade de São Paulo, Rua João Dagnone, 1100, São Carlos - Brasil

Abstract. *Unsteady simulations of the flow over generic high-lift airfoil configurations were carried out to investigate the sources of noise in the leading edge slat region using a Computational Fluid Dynamics code based on the Lattice-Boltzmann Method. Changes in the angle of attack and slat overlap were considered. The Proper Orthogonal Decomposition technique was used to educe the large scale structures in the slat region. Besides the conventional metrics based on the Turbulent Kinetic Energy, a correlation metrics based on the pressure fluctuations at a plane far from the slat region towards the ground was employed. Although the size of the recirculation zone inside the slat cove changed significantly with the angle of attack and overlap, the evolution of the spectrum of velocity fluctuations along the mixing layer followed the same pattern for all the cases simulated. However, great difference was observed in the spectrum of emitted noise. The large scale structures most correlated to the noise are two-dimensional and their shape suggests that they are related to the primary instability of the mixing layer. The dynamics of the dominant structures at the frequencies of the peaks are consistent with the occurrence of a pressure feedback mechanism acting inside the slat cove.*

1. INTRODUCTION

The noise generated by aircraft operations is of great concern given its harmful effect on comfort and health of the workers and the communities around the airports. With the introduction of the second generation, high by-pass ratio turbofan engines in commercial aircrafts, the airframe became relevant in the generation of external aircraft noise, mainly during approach and landing, since in these phases the propellers are in low power configurations. For regional, one-aisle aircrafts the slat becomes as relevant as the engines as external noise source [1].

For typical scaled wind-tunnel tests, the slat-generated noise spectrum commonly features three components: a hump at high frequency, a broadband portion ranging from low to intermediate frequencies and a series of narrowband peaks distinguished in the frequency range of maximum broadband noise [2]. Combination of wind-tunnel experiments and numerical simulations allowed the identification of coherent vortex shedding from the slat trailing edge as the mechanism behind the high frequency hump [3, 4]. On the other hand, the physics governing the other two features on the slat noise spectrum remains under discussion. Although it has been speculated that they are generically related to the growth of disturbances in a free shear layer inside the slat cove [5, 6], no precise mechanism was consistently proposed. It has been suggested that the series of peaks may be associated with resonance effects taking place at the slat cove [7] or to a mechanism of acoustic feedback typical of the flow over open cavities [8]. However, the success in relating such mechanisms to the details of the flow over the slat has been only partial.

The eduction of large scale structures based on data stemming from experiments of numerical simulations is a common approach in the investigations of the underlying physics of aeroacoustic noise generation [9]. The Proper Orthogonal Decomposition (POD) is a technique that optimally decomposes a set of data in a basis of orthonormal modes: in an averaged sense, the POD basis represents the set of realizations better than any other orthogonal basis with a given number of modes, for a predefined correlation metrics. Thus, it is important to define a correlation metrics that emphasize the particular features of the data that are more relevant to the problem to be studied.

The work described in this paper aims at studying the large scale structures in the slat region of a three-element high-lift geometry at different slat settings and airfoil angles of attack with focus on the generation of aeroacoustic noise. Comparing different conditions, it is possible to relate changes on the far-field noise spectrum to modifications in the turbulence in the slat region, particularly in the coherent fluctuations. Special attention is given to the structures related to the low-frequency peaks in the slat noise spectrum. To provide data of unsteady flow over the high-lift airfoil, a commercial code based on the Lattice-Boltzmann Method (LBM) was employed



Figure 1. Cross-section of the original MD30P30N high-lift airfoil.

2. UNSTEADY FLOW SIMULATIONS

2.1 Lattice-Boltzmann code

The simulations described in this paper are computed using the commercial code PowerFLOW 4.3a, which is based on the Lattice-Boltzmann method (LBM). It solves the discrete Boltzmann equation,

$$f(\vec{x} + \vec{c}\delta t, \vec{c}, t + \delta t) - f(\vec{x}, \vec{c}, t) = \Omega(f), \quad (1)$$

where the distribution function, $f(\vec{x}, \vec{c}, t)$, represents the odds to find a particle in the position \vec{x} with velocity \vec{c} at an instant t . The term Ω is called collision term and represents the exchange of momentum between the particles. For the flow conditions of interest to aeronautics, this term can be properly approximated by [10]:

$$\Omega(f) = -\frac{1}{\tau}(f - f^{eq}) \quad (2)$$

where τ is the relaxation time and f^{eq} is the equilibrium probability density function. The Boltzmann equation is discretized in a Cartesian mesh and solved explicitly in a volumetric formulation that enables the solution of problems with complex geometries [11]. The conservation equations and the perfect gas equation of state are retrieved by a Chapman-Enskog expansion, with the density ρ and macroscopic velocity \vec{U} given by

$$\rho(\vec{x}, t) = \sum_k f(\vec{x}, \vec{c}_k, t) \quad (3)$$

$$\rho(\vec{x}, t)\vec{U}(\vec{x}, t) = \sum_k \vec{c}_k f(\vec{x}, \vec{c}_k, t). \quad (4)$$

To calculate the effect of subgrid turbulence scales, the code uses a modified version of the k - ϵ turbulence model in its Renormalization Group (RNG) form. The calculation of the sound propagated to the far-field is made by means of the Farassat's formulation [12] of the Ffowcs Williams-Hawkings (FW-H) analogy [13]. The surface of integration of the Ffowcs Williams-Hawkings method corresponds to the slat surface and the surface of the aft half part of the main element. Tests were carried out to show that, for the Mach number used, the quadrupole sources are negligible [14].

3. Simulated models

The simulations considered high-lift configurations based on the three-element MD30P30N airfoil, whose cross-section is shown in Fig. 1, and the settings are described in Tab. 1. Besides the original, baseline MD30P30N configuration, two other slat settings were simulated (shown schematically in Fig. 2(a)), one with overlap equal to -2.95% of the stowed chord of 0.5m (in blue) and one with overlap 1.00% of the stowed chord (in green). The slat position in the baseline configuration is denoted by the black curve. The original configuration was simulated at two airfoil angles of attack, 4° and 8° , while the configurations with modified slat overlap were tested at 4° angle of attack (α).

Table 1. Geometrical settings of MD30P30N airfoil. Percentages are relative to the stowed chord.

	gap	overlap	deflection (δ)	chord
slat	2.95%	-2.50%	30°	15%
flap	1.25%	0.25%	30°	30%

The simulation model was scaled to match wind tunnel experiments [15], resulting in a Reynolds number of 1 million based on the stowed chord of the airfoil and free stream velocity, $U_\infty=34$ m/s, with a Mach number of $M=0.1$. The wind tunnel blockage effect was also taken into account by placing free-slip walls according to the tunnel dimensions.

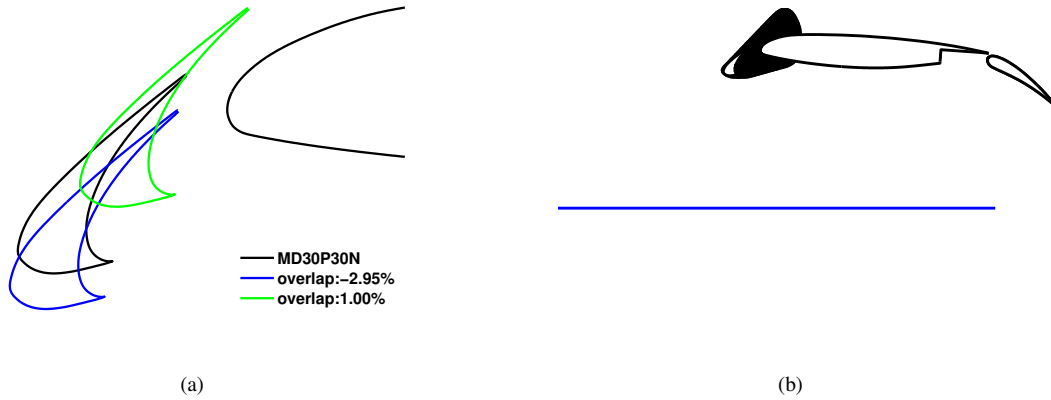


Figure 2. (a) Schematic view showing the slat position relative to the main element for the three configurations simulated. (b) Schematic view of the regions considered in the POD computations. Region in black: integration region for the TKE correlation metrics. Plane in blue: integration region for the acoustic pressure fluctuation metrics.

Periodicity is adopted in the boundary planes normal to the spanwise direction, which corresponds to the assumption of homogeneity in this direction. The simulated span was approximately 10% of the stowed chord.

For the original MD30P30N configuration at 4° angle of attack, simulations with two different grid definitions were carried out to assess the sensitiveness of the results to this model parameter. For the coarse grid configuration, the smallest elements had 0.2mm edge length. This mesh has a total of approximately 80 million elements. For the finer grid configuration, the smallest elements had edges of 0.14mm, resulting in a total of approximately 260 million elements.

All simulations were computed to comprise a physical time period of 0.30s. Analysis of time-averaged values and auto-correlation spectra indicated that this simulation time, after discarding the initial transient of 0.08s, is enough to achieve statistical convergence of the frequencies of interest.

4. PROPER ORTHOGONAL DECOMPOSITION

The Proper Orthogonal Decomposition (POD) is a correlation tool that decomposes a given set of empirical realizations, $\{q^i\}$, in an orthonormal, optimal basis $\{\phi_i\}$ [16]. The optimality of the basis means that, for a predefined correlation metric, there is no other orthogonal basis that better represents, on an average sense, the elements $\{q^i\}$ with a given finite number of modes than the basis formed by the elements $\{\phi_i\}$. Thus, the averaged projection of the flow realizations onto the POD basis must be maximized, leading to the eigenvalue problem

$$\mathbf{R}\phi = \lambda\phi, \quad (5)$$

where \mathbf{R} is the two-point cross-correlation matrix. The POD functions are ranked according to the POD eigenvalues λ_k , that serve as a measure (again, following the defined correlation metric) of the relative importance of the POD mode k in the flow. Our POD computations considered vector-valued flow realizations [17] in the time-spanwise Fourier domain, resulting in POD modes which were functions of the streamwise and vertical spatial coordinates and spanwise wavenumber and frequency. The computations were made by means of the Snapshot method [18] over a total 13 realizations for each time-spanwise Fourier component.

4.1 Correlation metrics

The choice of the correlation metric is an essential issue in the decomposition of the data with the POD technique. One must adopt a metric that highlights the features most relevant for her analysis. In the most general case, the inner product is written as

$$\langle \mathbf{a}, \mathbf{b} \rangle = \int_x \int_y \mathbf{b}^*(x, y) \mathbf{A}(x, y) \mathbf{a}(x, y) dx dy, \quad (6)$$

where the superscript $*$ denotes complex conjugate and $\mathbf{A}(x, y)$ is a matrix relating the different fluid variables in the vectors \mathbf{a} and \mathbf{b} . $\mathbf{A}(x, y)$ can also be used in order to give more importance to selected spatial regions.

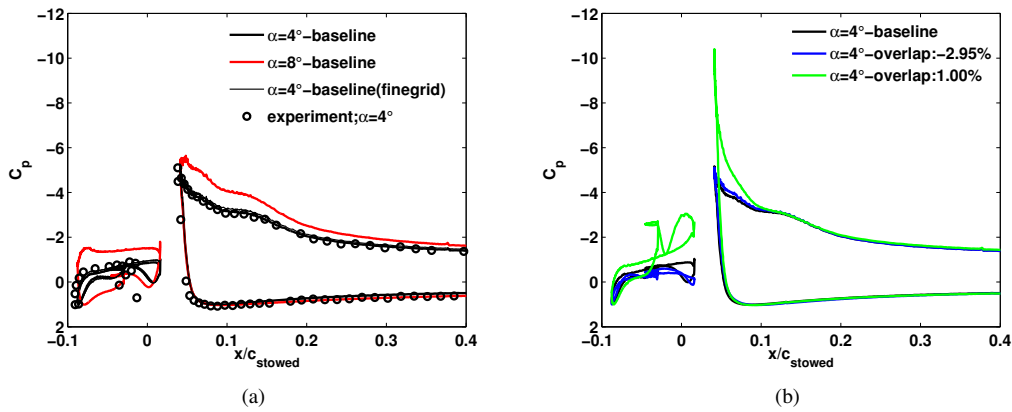


Figure 3. Mean pressure coefficient at the slat region for the cases simulated. (a) Comparison between 4° and 8° angle of attack for the baseline configuration and (b) comparison between three different slat overlap values for 4° angle of attack.

Two metric for the POD computations were considered here. The first one was based on the Turbulent Kinetic Energy (TKE), integrated over a portion of the domain containing the slat and the leading edge of the main element, which is schematically represented by the black region in Fig. 2(b). The second metric consisted on integrating the sound pressure intensity, proportional to the square of the pressure, along a horizontal plane below the airfoil, far from the noise source region (shown in blue in Fig. 2(b)). Its semi-norm is proportional to the acoustic intensity on the considered plane. The geometry of the regions in Fig. 2(b) correspond to the case with the original MD30P30N configuration at 4° angle of attack, but they were similar for the other three cases simulated. The spatial structures in the slat region identified by the POD modes according to the “far-field” pressure metric corresponds to the ones most correlated to the fluctuations in the far horizontal plane.

5. RESULTS

5.1 Flow characteristics and noise emission

Figure 3 shows the distribution of time-averaged pressure coefficient on the center plane of the computational model, displaying the effect of both the angle of attack for the original MD30P30N configuration and the effect of slat overlap. Figure 3(a) displays the results for the original configuration at 4° angle of attack based on the two grid configurations and wind tunnel measurements from [15]. We see that the simulation with the finer grid resulted in slightly more loaded elements in comparison to the coarser grid. However, this difference is marginal and both numerical simulations agree well with the measurements. For better visual comparison, in Fig. 3(b) the x coordinate of the slat for the -2.95% and 1.00% overlap cases was displaced to match the location of the slat in the baseline configuration. It can be seen that mean aerodynamics on the slat is greatly modified as the overlap is changed. Moreover, the effectiveness of the slat is substantially reduced as the overlap increases to 1.00% of the stowed chord, resulting in a strong suction peak on the main element.

The averaged field of Mach number in the slat region is shown in Fig. 4. In the mean velocity field, we can identify the recirculating zone in the slat cove as a portion of very low velocity flow. Just outside this zone, the flow is much faster and directed upwards to the slat gap. Therefore, a large velocity gradient is observed between this two flow regions. The white, dashed lines indicate the dividing streamlines at the mid-span for each case. Figure 5(a) shows profiles of the mean velocity along a line normal to the dividing streamlines at approximately 11% of their way from the cusp to the reattachment point. These mixing-layer-like profiles are capable of amplifying small disturbances in the flow due to their inflectional instability, being the major cause of turbulence inside the slat cove. The mixing-layer path (white, dashed lines in Fig. 4) for the four cases simulated are compared in Fig. 5(b). It is seen that as the angle of attack increases, the reattachment point moves away from the slat trailing edge and similarly, as the overlap increases, the distance between the reattachment point and the slat trailing edge increases.

Figure 6 shows the field of non-dimensionalized resolved Turbulent Kinetic Energy for the four cases simulated. It is seen that the mixing-layer disturbances grow and spread as they travel along the path towards the reattachment. In all cases, the maximum disturbance energy occurs at the reattachment region where the vortices are deformed and stretched. Based on the spectra of fluctuations of the streamwise velocity component, four main stages of evolution of the disturbances in the mixing-layer were identified for the four cases simulated. The spectra of streamwise velocity fluctuations at points representative of each stage are displayed in Fig. 7, as function of the Strouhal number based on the slat chord and free-stream velocity. In the first stage of the mixing-layer evolution broad humps appear and grow. Additionally, for the

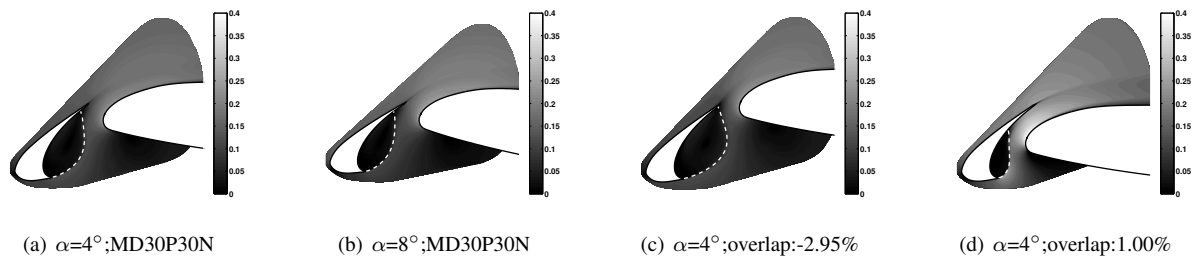


Figure 4. Contour plots of the Mach number field in the slat region. White, dashed lines denote streamlines leaving the cusp at $z=0$ and impinging on the slat lower surface.

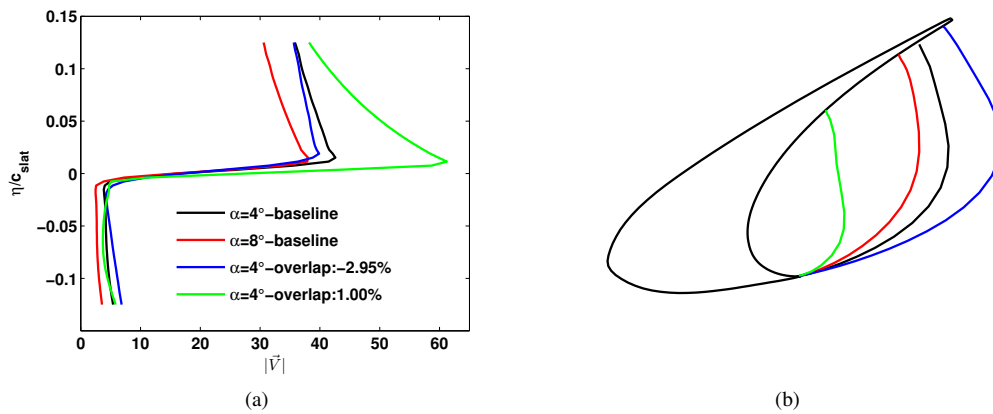


Figure 5. Mixing layer characteristics: (a) Mean velocity profile at approximately 11% of the way to the reattachment and (b) mixing-layer path from the slat to the reattachment.

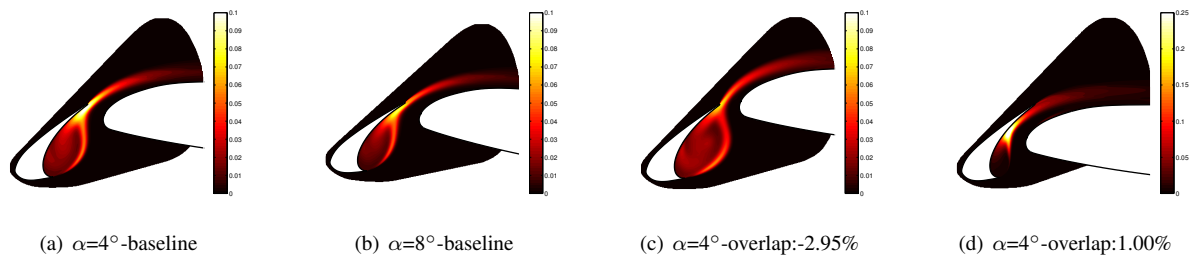


Figure 6. Field of resolved Turbulent Kinetic Energy in the slat region.

cases with negative overlap, a narrowband component start to appear at around $St=3$. This first stage takes place up to approximately 35% of the mixing-layer path for cases with overlap -2.50% and -2.95%, and 20% of S_{max} for the 1.00% overlap case. In the second stage, the amplitude of the humps grows substantially and the narrowband component of the cases with negative overlap, is damped. The second stage happens between 35% and 50% of the mixing-layer path for baseline and -2.95% overlap cases and between 20% and 30% for the 1.00% overlap case. In the third stage, between 50% and 70% for baseline configuration, between 50% and 63% for the case with overlap of -2.95% and between 30% and 67% for the case with overlap of 1.00%, fluctuations at frequencies below the frequency of the strongest hump amplify. For the cases with negative overlap, these low frequencies are marked by the presence of a series of narrowband peaks, including one at the same frequency as the peak damped during stage 2. For the case with 1.00% overlap, the spectrum has a more broadband character, compared to the others, although some peaks of lower amplitude can be seen in the spectrum of its third stage. The last stage, up to the reattachment, is characterized by the damping of the humps and peaks until the spectrum becomes basically broadband, with small remnants of the narrowband peaks.

The spectra of far-field noise computed by FW-H algorithm for the four cases studied are compared in Fig. 8. For the original MD30P30N configuration at $\alpha=4^\circ$, Fig. 8(a) compares the results of two grid configurations to wind tunnel measurements. From the spectra for all the cases, except the one with overlap 1.00% of the airfoil stowed chord, it is possible to identify the series of low frequency peaks typical of the noise emitted by wind tunnel slat models. For the baseline configuration at 4° angle of attack we can see that, as the spatial grid is refined, the amplitude of two of these

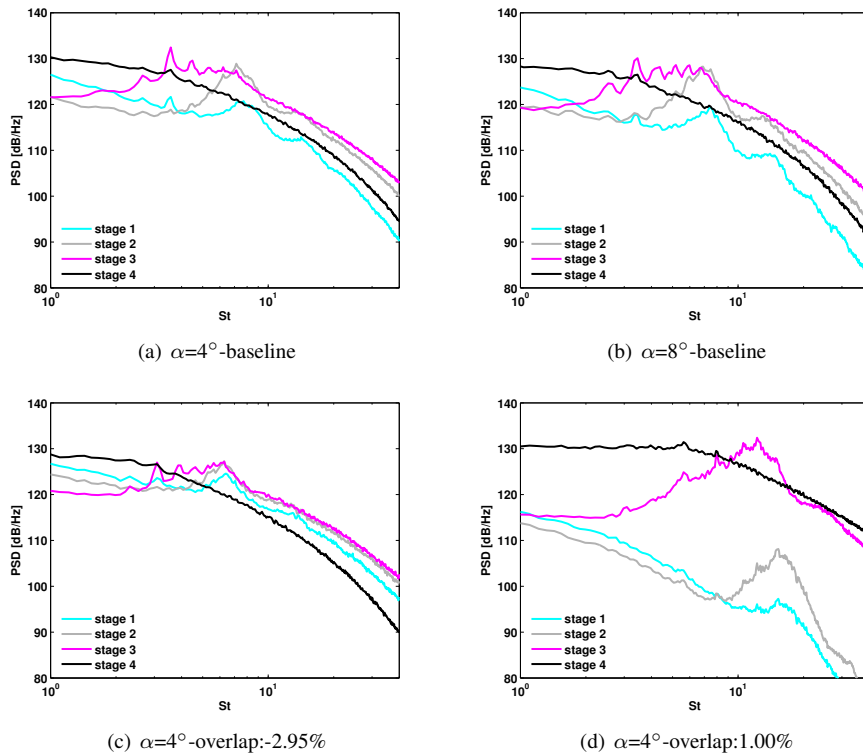


Figure 7. Power Spectral Density of the streamwise velocity component at selected points showing the stages of evolution of the slat mixing-layer disturbances.

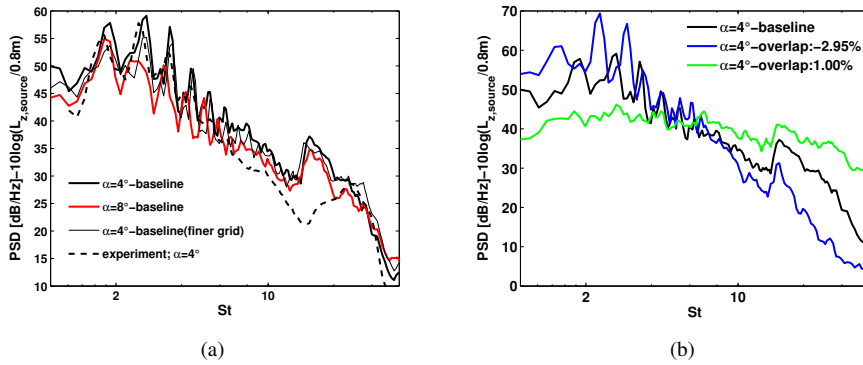


Figure 8. Power Spectral Density of the acoustic fluctuations calculated with Ffowcs Williams-Hawkings analogy for a listener at a point corresponding to the center of the microphone array used in the reference experiments [15].

peaks decreases slightly. However, the frequencies and amplitudes of the peaks predicted by both meshes compare well with the measurements. It is seen that, as the airfoil angle of attack and the overlap increases, the amplitude of the series of narrowband peaks decreases.

5.2 Large scale structures in the slat cove

Spectra of normalized POD eigenvalues based on the TKE metric for the baseline configuration at $\alpha=4^\circ$ are shown in Fig. 9 as function of the spanwise wavenumber, β , and the eigenfunction order, N . The eigenvalues are normalized by the sum of all eigenvalues for the given frequency, i.e., for each surface plot, we have $\sum_{\beta} \sum_N \Lambda_{\beta}^N = 1$. The Strouhal number 2.10 corresponds to a deep in the noise spectrum while $St=2.76$ corresponds to the frequency of one of the narrowband peaks. At the narrowband peak frequency $St=2.76$, the first mode for $\beta=0$ is the dominant mode, while the energy for the frequency of the deep in the noise spectrum is spread over the spanwise wavenumber range considered. Although not shown, for all cases simulated, the spectrum of POD eigenvalues based on the TKE metric for the frequencies of the narrowband peaks in the noise spectrum were dominated by the first two-dimensional ($\beta=0$) mode, while for the

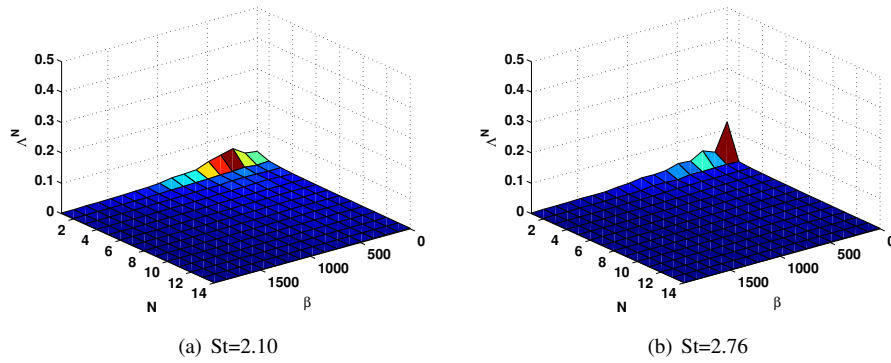


Figure 9. Spectra of POD eigenvalues considering the Turbulent Kinetic Energy metric for fluctuations at selected frequencies from the results of the the baseline configuration at $\alpha=4^\circ$. Strouhal number corresponds to a deep in the noise spectrum while 2.76 corresponds to a narrowband peak.

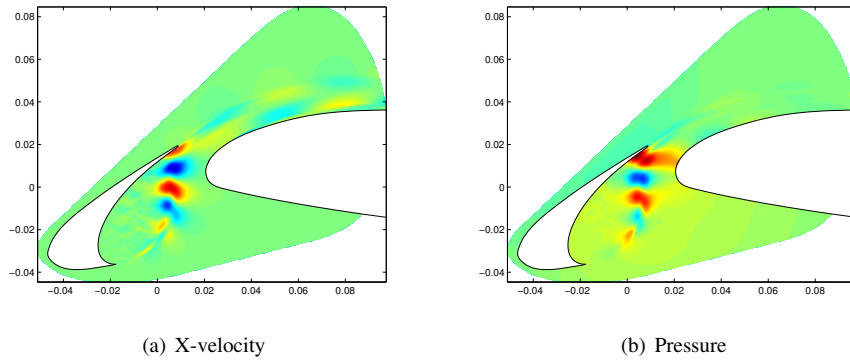


Figure 10. Real part of the first POD mode for fluctuations $(St;\beta)=(2.76;0)$, considering the Turbulent Kinetic Energy metric for the case $\alpha=4^\circ$ -baseline.

frequencies of deeps in the spectrum, three-dimensional modes dominated the spectra for the TKE metric.

The streamwise velocity and pressure components of the real part of the first TKE based POD mode with $\beta=0$ for $St=2.76$ are shown in Fig. 10. It is seen that the energy of the mode is predominantly located along the mixing-layer path and its shapes suggests that it represents the structures amplified due to the primary mixing-layer instability. The shape of the dominant modes corresponding the frequencies of the other peaks in the noise spectrum is similar to the one showed in Fig. 10 but with different instability wavenumber along the mixing-layer path.

Spectra of normalized POD eigenvalues based on the “far-field” pressure metric are shown in Fig. 11 for the same frequencies considered in Fig. 9, for the original MD30P30N configuration at 4° angle of attack. For this metric, the spectra of eigenvalues corresponding to frequencies of peaks and deeps in the noise spectrum are dominated by the first two-dimensional POD mode, this mode capturing typically 80% of the acoustic intensity in the far horizontal plane below the airfoil. This means that the pressure fluctuations outside the slat cove towards the ground are almost exclusively two-dimensional. Moreover, these fluctuations are highly coherent.

Figure 12 shows the streamwise velocity and pressure component of the real part of the dominant POD mode based on the “far-field” metric for $St=2.73$ for the baseline configuration at $\alpha=4^\circ$. As for the dominant modes at the peak frequencies based on the TKE metric, the shape of the mode in Fig. 12 suggests that it is dominated by the two-dimensional perturbations resulting from the primary mixing-layer instability. Although the dominant POD modes based on the “far-field” pressure fluctuation metric show a high correlation between these two-dimensional mixing-layer disturbances and the pressure fluctuations in a region below the airfoil, it does not necessarily imply a direct causal relation. For instance, the Ffowcs Williams-Hawkings computations compared well with wind tunnel measurements without considering the quadrupole sources represented by the unsteadiness in the flow itself. So, it is more likely that the noise is a result of the interaction between the structures identified in Fig. 12 and the surface of the slat and/or leading edge of the main element.

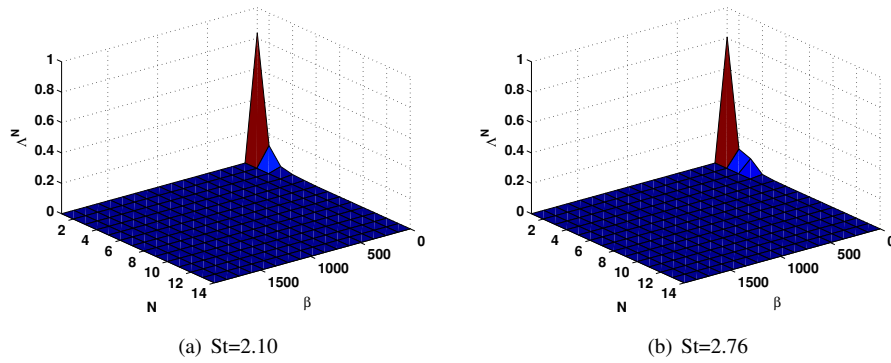


Figure 11. Spectra of POD eigenvalues considering “far-field” pressure norm for fluctuations at selected frequencies from the results of the case $\alpha=4^\circ$ -baseline. Strouhal number 2.10 corresponds to a deep in the “far-field” noise spectrum while 2.76 corresponds to a narrowband peak.

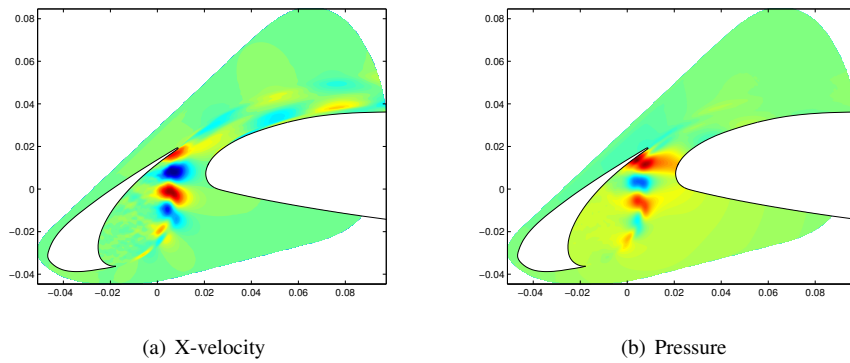


Figure 12. Real part of the first POD mode for fluctuations $(St;\beta)=(2.76;0)$, considering the “far-field” pressure metric for the case $\alpha=4^\circ$ -baseline.

5.3 Evidence of a pressure feedback loop

As shown in the last section, the structures inside the slat cove which are most correlated to the pressure fluctuations towards the ground are the perturbations amplified by the primary mixing-layer instability, either for the frequencies of the peaks or for the frequencies of deeps between peaks in the spectrum of noise. Therefore, it is not possible to understand why some frequencies are preferred over others only by looking at the shape of the POD modes. The hypothesis that a feedback mechanism is responsible for the selection of the series of narrowband peaks in the slat noise spectrum was investigated using the dominant POD modes based on the pressure fluctuations outside the cove. A cycle as defined by [8] was considered, which is described in Fig. 13. At the time $t=0$, the loop starts with the arrival of a pressure wave front A_0 at the slat cusp, exciting the mixing-layer (Fig. 13(a)). The disturbance introduced in the cusp grows, originating a discrete spanwise vortex V_1 , as it is convected along the mixing-layer path towards the reattachment, as shown in Fig. 13(b). At time $t=T_v$, V_1 impinges on the slat lower surface generating a new pressure wave front, A_1 (Fig. 13(c)). Since the flow velocity inside the recirculating zone is very low, the wave generated at the reattachment point travels approximately at the sound speed, c , towards the cusp, covering a distance L_a in a time interval $T_a=L_a/c$. At the time $t=T_v+T_a$, the wave front arrives at the cusp restarting the cycle. Following this chain of events, one wave front is emitted every interval of T_v+T_a , resulting in a fundamental frequency equal to $(T_v + T_a)^{-1}$. One can also think of a loop in which, between the departure of the disturbance from the cusp and its arrival at the reattachment point, another vortex shocks with the slat surface, emitting an acoustic wave. In this case, between $t=0$ and $t=T_v$, two vortices interact with the slat lower surface and, between $t=0$ and $t=T_v+T_a$, two wave fronts interact with the cusp, resulting in an acoustic emission of frequency $2(T_v + T_a)^{-1}$. Further modes with n vortices reaching the reattachment point between $t=0$ and $t=T_v$ also occur, resulting in emission of frequencies $n(T_v + T_a)^{-1}$.

To search for a relation between the structures identified by the POD modes and the feedback loop, the evolution in time of these POD modes was evaluated along the mixing-layer path and the straight line with length L_a , connecting the reattachment point to the cusp (see Fig. 13(b)). Figure 14 shows the pressure component of the real part of the spatio-temporal evolution of the first “far-field” based POD mode with $(St;\beta)=(3.53;0)$, along the mixing-layer path (Fig. 14(a)),

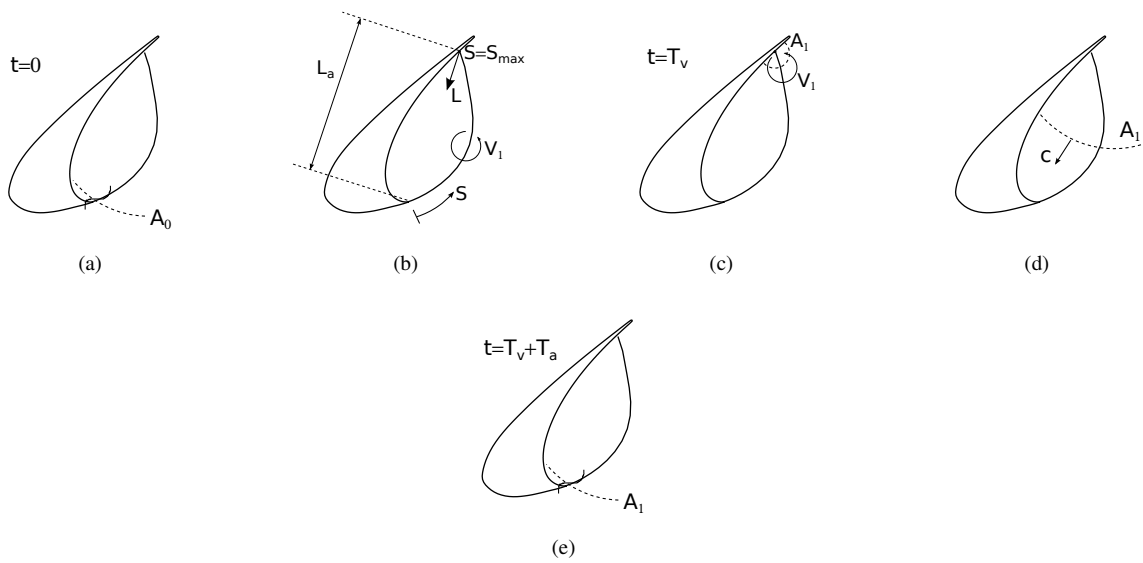


Figure 13. Schematic representation of the acoustic feedback loop inside slat cove representing the fundamental feedback mode ($n=1$).

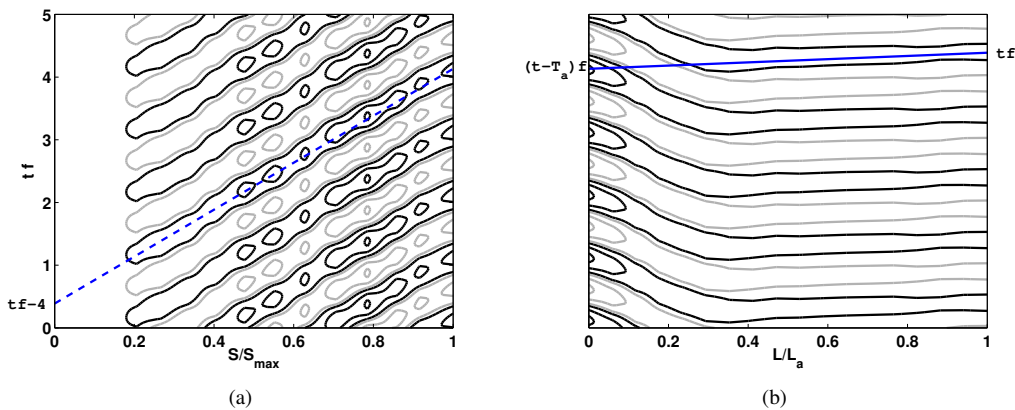


Figure 14. Space-time contour plot of the real part of the evolution of the $(St; \beta)=(3.53; 0)$ POD mode along (a) the mixing-layer path and (b) the straight line connecting the reattachment point to the cusp for the baseline configuration at $\alpha=4^\circ$. Combination of the dashed with the solid blue line represent a feedback mode of order $n=4$.

and along the straight line from the reattachment to the cusp (Fig. 14(b)), for the original configuration at 4° angle of attack. Black contours denote positive values, while gray contours denote negative values, and the vertical axis represents the product between time and the frequency of the mode. The solid, blue line is defined as a straight line connecting a pressure maximum at $L/L_a=1$ (cusp), at an instant t , to the point $L=0$ (reattachment), at the instant $t - T_a$, being T_a the time for an acoustic wave to travel from the reattachment point to the cusp. The dashed, blue line in the S/S_{max} versus t, f plot connects the point for $S/S_{max}=1$ (reattachment) at the time $t - T_a$ to a point for $S/S_{max}=0$ at an instant $t-4f^{-1}$. Thus the combination of the dashed and solid lines in Fig. 14(a) and 14(b), represents the cycle of a possible feedback mode mode of order $n=4$. It is seen that the evolution of the pressure component of the POD mode in the mixing-layer path closely represents the evolution for a possible $n=4$ feedback mode. Moreover, the solid line seems to be parallel to the evolution of the pressure component in the path L after $L/L_a \sim 0.3$.

6. CONCLUSIONS

Unsteady numerical computations of the flow on high-lift airfoil configurations were carried out using a Lattice-Boltzmann based code. Four conditions were simulated, considering variations of the airfoil angle of attack and slat overlap. The results showed limited sensitivity to the spatial grid resolution and good agreement with wind tunnel measurements. The position of the reattachment of the mixing layer on the surface of the slat cove changed significantly among the conditions tested. However, the evolution of the fluctuation spectra along the mixing layer followed basically

the same four stages for the four conditions analyzed. Analyses of the large scale structures inside the slat cove with the Proper Orthogonal Decomposition technique based on the Turbulent Kinetic Energy showed that the coherent fluctuations at the frequency of the peaks are predominantly two-dimensional, while at frequencies of deeps between peaks, the coherent fluctuations are typically three-dimensional. On the other hand, the POD computations based on the sound intensity far from the turbulent flow within the slat cove showed that the pressure unsteadiness emerging from the cove for the conditions tested is basically two-dimensional, for frequencies corresponding to peaks and deeps in the noise spectrum. Inspection of the shape of POD modes showed that the turbulent structures inside the cove which are more correlated to the most coherent pressure fluctuations in the “far-field” resembles the shape of disturbances caused by the primary instability of the mixing layer. The time evolution of the dominant POD mode at the frequencies of the narrowband peaks was shown to be consistent with the steps of a model for a pressure feedback loop in the slat cove.

7. ACKNOWLEDGEMENTS

D.S.S. received funding from CAPES, Coordenação de Aperfeiçoamento de Pessoal de Nível Superior. D.R. also acknowledge support from CAPES, Coordenação de Aperfeiçoamento de Pessoal de Nível Superior - Brasil, in the scope of the Program Ciências sem Fronteiras - CsF. M.A.F.M. acknowledge support from FAPESP, Fundação de amparo à pesquisa do estado de São Paulo and CNPq, Conselho Nacional de Desenvolvimento Científico e Tecnológico. The authors are also thankful to EMBRAER for the license of the LBM code and the Núcleo de Dinâmica do Fluidos.

8. REFERENCES

- Dobrzynski, W.,2010, “Almost 40 years of airframe noise research:What did we achieve?”, *Journal of Aircraft*, Vol.47, Nr. 2, pp. 353-367.
- Imamura, T. , Ura, H. , Yokokawa, Y. , Yamamoto, K., 2009, “A Far-Field Noise and Near-Field Unsteadiness of a Simplified High-Lift-Configuration Model (Slat)”, *AIAA Paper* 2009-1239.
- Khorrani, M. , Berkman, M. , Choudhari, M.,2000, “Unsteady flow computation of a slat with a blunt trailing edge”, *AIAA Journal*, Vol.38, Nr. 11, pp. 2050-2058.
- Choudhari, M. , Lockard, D. , Macaraeg, M. , Singer, B. , Streett, C. , Neubert, G. , Stoker, W. , Underbrink, J. , Berkman, M. , Khorrani, M. , Sadowski, S., 2002, “Aeroacoustic experiments in the Langley Low-Turbulence Pressure Tunnel”, *NASA Tech. Report*, Hampton, USA.
- Paschal, K. , Jenkins, L. , Yao, C.,2000, “Unsteady slat-wake characteristics of a high-lift configuration”, *AIAA Paper* 2000-0139.
- Khorrani, M. R. , Singer, B. , Berkman, M.,2001, “Time-accurate simulations and acoustic analysis of slat free-shear-layer”, *AIAA Paper* 2001-2155.
- Hein, S. , Hohage, T. , Koch, W. , Schöberl, J.,2007, “Acoustic resonances in a high-lift configuration”, *Journal of Fluid Mechanics*, Vol.582, pp.179-202.
- Terracol, M. , Manoha, E. , Lemoine, B.,2011, “Investigation of the unsteady flow and noise sources generation in a slat cove: hybrid zonal RANS/LES simulation and dedicated experiments”, *AIAA Paper* 2011-3203.
- Freund, J. , Colonius, T.,2009, “Turbulence and sound-field POD analysis of a turbulent jet”, *Int J Aeroacoustics*, Vol.8, pp.337-354.
- Bhatnagar, P. L. , Gross, E. P. , Krook, M.,1954, “A model for collision processes in gases. I. Small amplitude processes in charged and neutral one-component systems”, *Physical Review*, Vol.94, Nr. 3, pp.511-525.
- Chen, H. , Teixeira, C. , Molvig, K.,1999, “Realization of fluid boundary conditions via discrete Boltzmann dynamics”, *International Journal of Modern Physics C*, Vol.10, pp.1-11.
- Farassat, F. , Succi, G.,1980, “A review of propeller discrete frequency noise prediction technology with emphasis on two current methods for time domain calculations”, *Computers and Fluids*, Vol.35, pp.898-909.
- Brès, G. A. and Pérot, F. and Freed, D.,2010, “A Ffowcs Williams-Hawkings solver for lattice-Boltzmann based computational aeroacoustics”, *AIAA Paper* 2010-3711.
- Lockard, D. P. and Choudhari, M. M.,2009, “Noise radiation from leading-edge slat”, *AIAA Paper* 2009-3101.
- Pagani, Jr., C. and Souza, D. S. and Medeiros, M. A. F.,2016, “Slat Noise: Aeroacoustic Beamforming in Closed-Section Wind Tunnel with Numerical Comparison”, *AIAA Journal*, Accepted for publication.
- P. Holmes and J. Lumley and G. Berkooz,1996, “Turbulence, Coherent Structures, Dynamical Systems and Symmetry”, *Cambridge University Press*, Edinburgh, 420 p..
- Rowley, C., Colonius, T., Murray, R. ,2004, “Model reduction for compressible flows using POD and Galerkin projection”, *Computers and Fluids*, Vol.35, pp.898-909.
- Sirovich, L.,1987, “Chaotic dynamics of coherent structures. Parts I-III”, *Quarterly of Applied Mathematics*, Vol.45, Nr.3.

9. RESPONSIBILITY NOTICE

The author(s) is (are) the only responsible for the printed material included in this paper.